

PAPER

# Data-Driven Modeling of Photosynthesis Regulation Under Oscillating Light Condition - Part I: In-Silico Exploration

Christian Portilla,<sup>1</sup> Arviandy G. Aribowo <sup>1</sup>, Ramachandran Anantharaman <sup>1</sup>,  
César A. Gómez-Pérez <sup>1</sup> and Leyla Özkan <sup>1,\*</sup>

<sup>1</sup>Department of Electrical Engineering, Eindhoven University of Technology, P.O.Box 513, 5600 MB, Eindhoven, The Netherlands

\*Corresponding author. lozkan@tue.nl

## Abstract

This paper explores the application of data-driven system identification techniques in the frequency domain to obtain simplified, control-oriented models of photosynthesis regulation under oscillating light conditions. In-silico datasets are generated using simulations of the physics-based Basic DREAM Model (BDM) Fuente et al. [2024], with light intensity signals—comprising DC (static) and AC (modulated) components as input and chlorophyll fluorescence (ChlF) as output. Using these data, the Best Linear Approximation (BLA) method is employed to estimate second-order linear time-invariant (LTI) transfer function models across different operating conditions defined by DC levels and modulation frequencies of light intensity. Building on these local models, a Linear Parameter-Varying (LPV) representation is constructed, in which the scheduling parameter is defined by the DC values of the light intensity, providing a compact state-space representation of the system dynamics.

**Key words:** Photosynthesis regulation, Oscillating light, Frequency-domain system identification, Best linear approximation, Linear-parameter varying model.

## Introduction

Cultivating plants demands vast resources—about 70% of all water used in Spain, and roughly 7% of national energy consumption for greenhouses in the Netherlands. With mounting environmental and other pressures, current cultivation practices are under strain. A major challenge for the coming decades is to deploy breakthrough, high-throughput technologies to improve plants—both with and without genome engineering—and to enable more resource-efficient cultivation. This is the vision behind DREAM, an EU-funded, science-driven technology initiative.<sup>1</sup>

To optimize plant growth, it is desirable to enhance lighting efficiency Baker [2008], which can be performed by dynamically modelling and optimizing the light acclimation of photosynthetic organisms. The aim is to exploit mathematical models to tailor time-modulated illuminations such that they can optimize the photon budget (enhanced lighting efficiency) for driving photosynthesis (i.e., in controlled environments). However, actual light optimization requires the understanding and prediction of photon used by PSII. In order to achieve these goals, the DREAM consortium is undertaking experimental studies with organisms, such as algae and tomatoes, and also developing dynamic models (based on the first-principle

and experimental data) to study the photosynthesis regulation under modulated light conditions.

Photosynthesis is a complex process that strongly influences plant behavior. It involves mechanisms operating on different time scales, ranging from fast dynamics in light harvesting to slow dynamics in the chemical synthesis of organic compounds for plant growth. Moreover, the photosynthetic process exhibits dynamic responses to unfavorable conditions or to its own physiological state, such as photorespiration Ogawa [1982], photoinhibition Eilers and Peeters [1988]; Wu and Merchuk [2001], and light acclimation processes Kenneth L. Denman [1986]. Developing a complete model of photosynthesis would require significant effort and extensive experimental data. A more practical approach is to focus on specific characteristic phenomena. The literature contains numerous models that aim to predict photosynthetic behavior. Some of these address: CO<sub>2</sub> assimilation in the Calvin cycle Pearcy et al. [1997], the activities of the Rubisco enzyme (associated with the consumption of CO<sub>2</sub> and O<sub>2</sub>) and the delayed CO<sub>2</sub> release during photosynthetic assimilation and photorespiration processes in leaves Roussel and Igarberdiev [2011], and light acclimation and photoinhibition under periodically changing light C. Pahl-Wostl [1990]. Light optimization and control in greenhouses are related to the light-harvesting function of photosystem II (PSII). The efficiency of light used by plants has been evaluated through chlorophyll fluorescence Baker [2008], which provides indirect measurements of photochemical and

<sup>1</sup> See more information about the EU-funded DREAM initiative project in <https://dream-eic.eu/>

non-photochemical quenching. This concept underpins the Basic Dream Model (BDM) developed for photosynthetic reactions that depend on light intensity oscillations between  $10^{-3}$  and  $10^3$  Hz, as reported in Fuente et al. [2024]. Here, the authors propose a mechanistic representation of electron transport in PSII and a dynamic model to predict photochemical and non-photochemical quenching under harmonically oscillating light. This model is suitable for light optimization; however, it remains too complex for control design purposes.

Oscillating light is closely related to photochemical and non-photochemical quenching mechanisms that plants have developed to enhance energy use. Examples of naturally occurring oscillating light patterns include leaf flutter and the movement of algal cells in turbulent flows. The study in Salvatori et al. [2022] introduced and validated a simple dynamic model that captures how photosynthesis responds to fluctuating light at the leaf level, bridging experimental data and theory. By highlighting differences between genotypes and emphasizing the role of dynamic processes like non-photochemical quenching (NPQ) and cyclic electron flow, it provides a foundation for scaling up to canopy-level models of photosynthesis in realistic environments. The works Nedbal and Lazár [2021], Lazár et al. [2022], Niu et al. [2023] pioneered the use of frequency-domain analysis (already well-established in the field of control systems) as an alternative approach in photosynthesis studies under oscillating light experiments. They reveal how plants regulate photosynthetic regulation and electron transport processes across different temporal scales, providing mechanistic insight into how photosynthesis is stabilized under natural, fluctuating light.

Understanding all these phenomena are fundamental for analysis of dynamical behavior of biochemical processes in plants, which leads to improved performance of associated reactions. Although various models have been proposed to describe the influence of oscillating light on photosynthesis, their inherently nonlinear mathematical structures often are too complex for practical applications of regulation of photosynthesis. For example, the nonlinear terms in these models can hinder development and use of standard control design tools for light modulation. Alternatively, system identification methods are a data-driven modeling approach that can capture key system dynamics with reduced complexity, offering a more practical route for investigating and optimizing photosynthetic processes.

System identification techniques, widely used in engineering and control theory, have not yet been broadly applied to study and analyze photosynthesis regulation in plants. Their integration could provide powerful tools to quantitatively model, predict, and control dynamic responses in photosynthetic systems, but this potential remains largely unexplored. For example, Bala et al. [2025] demonstrates that a data-driven system identification approach can effectively model plant chlorophyll fluorescence responses under dynamic light, bridging control engineering and plant physiology. By showing that black-box models can approximate biologically meaningful processes, it lays the groundwork for real-time phenotyping, stress detection, and digital twin applications in agriculture.

Advanced system identification techniques for nonlinear systems, such as the Best Linear Approximation (BLA) framework and Linear Parameter-Varying (LPV) models, have been extensively developed and refined in control engineering to capture nonlinearities, process noise, and varying operating conditions. However, these powerful data-driven approaches have not yet been systematically explored for modeling and analyzing photosynthesis regulation. The BLA method, see further in Dobrowiecki and Schoukens [2007], Pintelon and Schoukens [2013], Schoukens and van den Hof [2018], Schoukens and Ljung [2019], Schoukens et al. [2020], provides a systematic

way to approximate nonlinear systems by a linear model that best represents their dynamics under specific excitation conditions, while also quantifying nonlinear distortions and noise contributions. Its significance lies in enabling robust and interpretable models of nonlinear dynamics, serving as a bridge toward more complex nonlinear identification. While the LPV modeling framework (see, for example, Laurain et al. [2010], Lovera et al. [2013], Bachnas et al. [2014]), by contrast, generalizes linear system descriptions by allowing model parameters to vary with measurable scheduling variables, thus capturing a wide range of nonlinear and time-varying behaviors. This significantly enables scalable, data-driven representations of nonlinear systems that remain compatible with powerful linear control and identification tools, making it highly suitable for complex biological regulation problems.

In this paper, we present modeling results demonstrating the application of a frequency-domain system identification approach (i.e., in terms of transfer functions) that capture the input–output dynamics of photosynthetic regulation. The main contributions of this work can be summarized as follows:

1. Application of BLA for local modeling: We employ the BLA method on in-silico input–output data generated from BDM simulations to construct local transfer function models under varying operational conditions. These conditions are defined by the input (light intensity) dynamics, including DC/constant levels as well as modulation frequencies and amplitudes.
2. Development of an LPV representation: Building on the local models, we develop a Linear Parameter-Varying (LPV) representation in which the scheduling parameter is defined by the operational range of DC light intensity values, thereby enabling a compact, global model description across multiple operating regimes.

Overall, these contributions provide an advanced data-driven approach for quantitatively characterizing regulatory mechanisms in photosynthesis. This paper also provides a concise tutorial on the application of system identification technique commonly used in the control systems community

The remainder of this paper is structured as follows. Section 2 introduces briefly the BDM as the foundation for generating in-silico input–output data. Section 3 details the application of the BLA method for deriving local transfer function models under varying light conditions. Section 4 then presents the construction of an LPV representation to capture system behavior across operating regimes. Finally, Section 5 summarizes the key findings and discusses an outlook for future research on system identification in photosynthesis regulation.

## Basic DREAM Model (BDM)

The Basic Dream Model (BDM) represents dynamical systems of photosynthetic reactions under the influence of light intensity oscillations within the frequency range of  $10^{-3} - 10^3$  Hz Fuente et al. [2024]. The BDM is described by a set of nonlinear ordinary differential equations (ODE), which can be formed as the following state and output equations (i.e., also known as the state-space form):

$$\dot{\mathbf{x}}(t) = f(\mathbf{x}(t), u(t), \Phi), \quad (1a)$$

$$\mathbf{y}(t) = g(\mathbf{x}(t), u(t), \Phi). \quad (1b)$$

where the state variables  $\mathbf{x}(t) \in \mathbb{R}^5$  with

- $x_1(t) = \text{PQ}(t)$  for the oxidized plastoquinone pool,

- $x_2(t) = H_L(t)$  for the proton concentration in the thylakoid lumen,
- $x_3(t) = FQ_{act}(t)$  for the active fraction of the photosystem II quencher,
- $x_4(t) = ATP(t)$  for the ATP concentration in the stroma,
- $x_5(t) = PI_{ox}(t)$  for the photosystem I donors that accept electrons from the plastoquinone pool.

The vector field  $f(\cdot)$  in Eq. (1a) describes the evolution of the state vector  $\mathbf{x}(t)$ . The vector field  $g(\cdot)$  in Eq. (1b) gives the trajectory of the output vector  $\mathbf{y}(t)$ ; see further details about these vector fields in Appendix A. The input signal  $u(t) = L(t)$  is the light intensity composed of two components as follows: the DC/static signal and the modulation signal (in terms of the amplitude and frequency of light oscillation). The output vector  $\mathbf{y}(t) \in \mathbb{R}^3$  is composed by

- $y_1(t) = \text{ChlF}$ , for the chlorophyll fluorescence yield,
- $y_2(t) = \text{NPQ}$ , for the non-photochemical quenching,
- $y_3(t) = \frac{dO_2}{dt}$ , for the rate of oxygen evolution due to the water splitting in PSII.

This study considers only the chlorophyll fluorescence output  $y_1(t)$  to generate in-silico data for system identification, as detailed in the next section. For simplifying the notation, now we write the chlorophyll fluorescence output  $y_1(t)$  as  $y(t)$ .

## Frequency-domain system identification: Best Linear Approximation (BLA) method

Section 3.1 details the methodology for obtaining the Frequency Response Function (FRF) for the BDM using nonparametric frequency domain analysis. Combined with carefully designed excitation signals, this approach effectively separates noise from nonlinearities. Furthermore, Section 3.2 focuses on identifying a parametric model within the frequency domain based on the nonparametric analysis.

### Non-parametric analysis

#### The Frequency Response Function (FRF)

The FRF represents the relationship between the input and the output in the frequency domain and is an experimental (data) representation of the transfer function  $G(j\omega)$ . For linear systems, the transfer function  $G(j\omega)$  is given by:

$$G(j\omega) = \frac{Y(j\omega)}{U(j\omega)}, \quad (2)$$

where  $Y(j\omega)$  and  $U(j\omega)$  are the Fourier transform (FT) of the output signal  $y(t)$  and the input signal  $u(t)$ . For a periodic excitation signal  $u(t) = A \sin(\omega t + \phi)$  with frequency  $\omega$  and phase  $\phi$ , the output is calculated as:  $y(t) = |G(j\omega)| A \sin(\omega t + (\phi + \angle G(j\omega)))$ , where  $|G(j\omega)|$  and  $\angle G(j\omega)$  are the magnitude and phase of  $G(j\omega)$ , respectively. However, photosynthetic organisms exhibit non-linear dynamical behavior, and the fluorescence measurements are affected by noise. In this case, Eq.(2) can be rewritten as follows:

$$Y(k) = G(j\omega) U(k) + \sigma_{NL}^2(k) + \sigma_n^2(k), \quad (3)$$

where  $\sigma_{NL}^2(k)$  and  $\sigma_n^2(k)$  represent the distortions caused by nonlinearities and noise, respectively.

#### Multi-frequency (multisine) excitation

The frequency response function (FRF) can be obtained using stepped sine signals, where the system is excited by varying the

light intensity according to a sinusoidal function,  $\sin(2\pi f t)$ , at a modulation frequency  $f$  at a time instant  $t$ . However, this approach is time-consuming because transients must reach steady state before data can be collected at each subsequent frequency. As a more efficient alternative, multi-frequency (multisine) excitation signals can be used, comprising a set of  $F$  frequencies and defined as follows:

$$u(t) = u_{dc} + \sum_{k \in F} A_k \sin(2\pi f_k t + \phi_k), \quad (4)$$

where  $A_k$ ,  $f_k$ , and  $\phi_k$  are the amplitude, frequency, and phase of the modulation, respectively. The frequencies in the set  $F$  can be uniformly distributed in the frequency range of interest or follow a logarithmic distribution, depending on the desired resolution. When the amplitudes  $A_k$  are set equal for all frequencies in the set  $F$ , the signal power is uniformly distributed throughout the frequency spectrum. A DC offset  $u_{dc}$  was added to ensure nonnegative light intensity.

In the simulation,  $u_{dc}$  was tuned to enhance signal power with minimal oscillations, for example, using the modulation amplitude  $A_k = 38 \mu\text{Em}^{-2}\text{s}^{-1}$  and  $F = 30000$  frequencies uniformly distributed from  $10^{-4}$  to 10 Hz as in the magnitude plot Figure 1. Note that the modulation amplitudes in this magnitude plot are identical in all frequencies. Furthermore, the phases  $\phi_k$  are randomly assigned to avoid large amplitude peaks in the multisine signal, thereby reducing the crest factor and improving the noise-to-signal ratio (NSR). A detailed discussion of crest factor analysis is provided in Pintelon and Schoukens [2012], Schoukens et al. [2012].

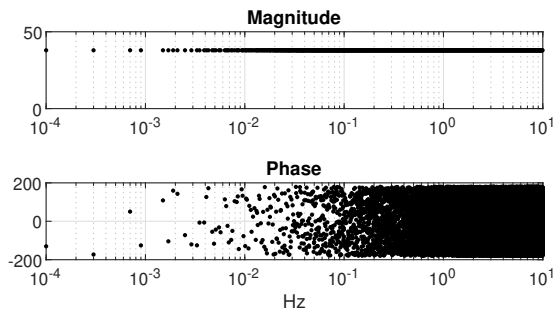


Fig. 1. Spectrum of multisine signal with random phase and amplitude of  $38 \mu\text{Em}^{-2}\text{s}^{-1}$  Pintelon and Schoukens [2012], Schoukens et al. [2012].

#### Noise and nonlinear distortions characterization

Using non-parametric frequency domain analysis, we obtained the Frequency Response Function (FRF) through carefully designed excitation signals, which separated noise from nonlinearities. Discriminating between these requires careful experimental planning, especially by selecting excitation signals. Periodic signals are particularly useful during non-parametric preprocessing (without considering interactions), as they allow the calculation of the FRF, noise power spectrum, and nonlinear distortions Schoukens and Ljung [2019]. Note that we focus on nonlinear PISPO (Period-In, Same-Period-Out) systems, where the steady-state response to a periodic input is expected to produce an output signal within the same period.

To characterize the noise, the system should be excited for at least two periods after reaching a steady state. This method is effective because, while noise varies between periods, nonlinear distortions remain consistent Schoukens and Ljung [2019].

Let us consider a system  $y(t) = f(u(t))$  excited with a periodic signal  $u(t)$  during  $P$  periods in steady-state conditions. The Discrete Fourier Transform (DFT) is calculated for the input and output of each period, obtaining  $U^{[l]}(k)$ ,  $Y^{[l]}(k)$ , for  $l = 1, \dots, P$ . The sample mean for each experiment  $\hat{Y}(k)$  and noise variance  $\sigma_Y^2(k)$  are given by:

$$\hat{Y}(k) = \frac{1}{P} \sum_{l=1}^P Y^{[l]}(k), \quad (5)$$

$$\sigma_Y^2(k) = \frac{1}{P-1} \sum_{l=1}^P |Y^{[l]}(k) - \hat{Y}(k)|. \quad (6)$$

Nonlinearities can be assessed by repeating the experiment using different realizations of random-phase multisine excitation. To quantify nonlinearities, the principle involves calculating the variance,  $\sigma_{NL}^2(k)$ . In linear systems, the phase relationship between input and output remains constant. Using this property and generating multiple realizations of random phase multisine signals, the variance can be used to estimate non-linear distortions. In general, for the FRF for the experiment  $m$  is given by:

$$G^{[m]}(j\omega_k) = \frac{\hat{Y}^{[m]}(k)}{\hat{U}^{[m]}(k)}. \quad (7)$$

For a set of  $M$  experiments using  $M$  realizations of a random phase multisine signal, the Best Linear Approximation (BLA) is given by Pintelon and Schoukens [2012], Schoukens et al. [2012]

$$G_{BLA}(j\omega_k) = \frac{1}{M} \sum_{m=1}^M G^{[m]}(j\omega_k). \quad (8)$$

The total distortion, accounting for both nonlinearities and noise, can then be calculated as follows:

$$\sigma_{G_{BLA}}^2(j\omega_k) = \sum_{m=1}^M \frac{|G^{[m]}(j\omega_k) - G_{BLA}(j\omega_k)|^2}{M(M-1)}. \quad (9)$$

Applying the multisine light intensity shown in Figure 1 and adding a DC value of  $100\mu E, m^{-2}, s^{-1}$ , the variance between the last four periods (during the steady state) and the six realizations of the multisine signal can be calculated. This discriminates FRF and non-linear behavior, as illustrated in Figure 2. Note that this example has no noise, as each period is identical to the others. This is because the data are derived from a simulation of the BDM.

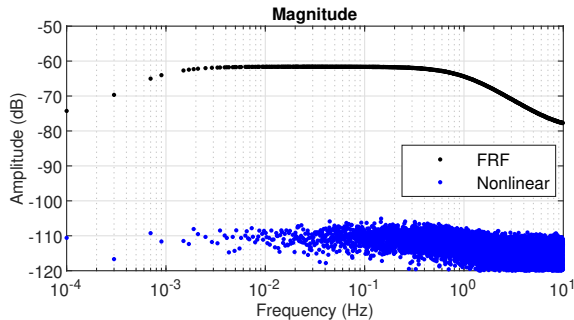


**Fig. 2.** Magnitude spectrum of fluorescence in response to multisine light intensity with an amplitude of  $38\mu E, m^{-2}, s^{-1}$  and a DC value of  $100\mu E, m^{-2}, s^{-1}$ . The plot distinguishes between linear and nonlinear behavior.

Figure 2 shows that the separation between the Frequency Response Function (FRF) and the nonlinearities exceeds 40 dB, indicating

that the linear contribution is 100 times stronger than the nonlinearities across all frequencies.

## Parametric analysis

For performing parametric identification in the frequency domain (see further in Pintelon and Schoukens [2012], Schoukens et al. [2012]), consider that a transfer function  $G(z_k)$  at frequency  $k2\pi/N$  is given by:

$$G(z_k) = \frac{Y(k)}{U(k)} = \frac{B(z_k)}{A(z_k)} = \frac{\sum_{l=0}^{n_b} b_l z_k^{-l}}{\sum_{l=0}^{n_a} a_l z_k^{-l}}, \quad (10)$$

with  $z_k$  being the discrete domain frequency variable at frequency  $kf_0$ . The objective is to find the polynomial coefficients of  $B(z_k)$  and  $A(z_k)$  (i.e., the values of  $b_k$  and  $a_k$ ) and approximate the polynomial degrees  $n_b$  and  $n_a$ .

$$\begin{aligned} a_0 Y(k) + a_1 Y(k) z_k^{-1} + \dots + a_{n_a} Y(k) z_k^{-n_a} = \dots \\ \dots b_0 U(k) + b_1 U(k) z_k^{-1} + \dots + b_{n_b} U(k) z_k^{-n_b}. \end{aligned} \quad (11)$$

Assuming  $a_0 = 1$ , a static set of complex equations can be constructed as:

$$\underbrace{\begin{bmatrix} Y(0) \\ \vdots \\ Y(N/2) \\ \vdots \\ U(0) \\ \vdots \\ U(N/2) \\ \vdots \\ U(0) z_0^{-n_b} \\ \vdots \\ U(N/2) z_{N/2}^{-n_b} \end{bmatrix}}_{\mathbf{Y}} = \underbrace{\begin{bmatrix} Y(0) z_0^{-1} & \dots & Y(N/2) z_{N/2}^{-1} \\ \vdots & \ddots & \vdots \\ Y(0) z_0^{-n_a} & \dots & Y(N/2) z_{N/2}^{-n_a} \\ U(0) & \dots & U(N/2) \\ \vdots & \ddots & \vdots \\ U(0) z_0^{-n_b} & \dots & U(N/2) z_{N/2}^{-n_b} \end{bmatrix}}_{\mathbf{K}} \underbrace{\begin{bmatrix} a_1 \\ \vdots \\ a_{n_a} \\ b_0 \\ \vdots \\ b_{n_b} \end{bmatrix}}_{\boldsymbol{\theta}}. \quad (12)$$

The linear system above is given by  $\mathbf{Y} = \mathbf{K}\boldsymbol{\theta}$ , where  $\boldsymbol{\theta}$  represents the vector of unknown parameters. The previous complex system can be transformed into a real-valued system by:

$$\begin{bmatrix} \text{real}(\mathbf{Y}) \\ \text{imag}(\mathbf{Y}) \end{bmatrix} = \begin{bmatrix} \text{real}(\mathbf{K}) \\ \text{imag}(\mathbf{K}) \end{bmatrix} \boldsymbol{\theta}. \quad (13)$$

Then, the previous system  $\mathbf{Y}_{\text{real}} = \mathbf{K}_{\text{real}} \boldsymbol{\theta}$  can be solved using Least Squares (LS) as:

$$\boldsymbol{\theta} = (\mathbf{K}_{\text{real}}^T \mathbf{K}_{\text{real}})^{-1} \mathbf{K}_{\text{real}}^T \mathbf{Y}_{\text{real}}. \quad (14)$$

At this stage, the user must decide on the complexity of the linear model by selecting the degrees of  $B(z_k)$  and  $A(z_k)$ , that is, determining precisely the values of  $n_b$  and  $n_a$ . Generally, a good model adheres to the principle of parsimony, achieving the highest possible accuracy with the fewest parameters. In this regard, we choose the following polynomial degrees:  $n_b = n_a = 2$ . As a result, a second order model is derived from the nonparametric analysis presented in Figure 2. The magnitude spectra of the parametric (also called the magnitude bode plot) and nonparametric models are shown in Figure 3. The Least Squares approximation fails for frequencies below  $10^{-3}$  Hz due to the scarcity of data points at these frequencies. Consequently, the solution neglects this frequency range.

A weighted version of the Least Squares (WLS) method is implemented to address the scarcity of data issue mentioned above, with an increased emphasis on lower frequencies. Consequently, Eq. (14) can be rewritten as follows:

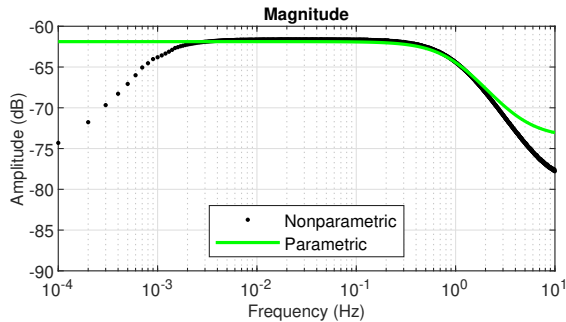


Fig. 3. Comparison of nonparametric and parametric (LS) models for fluorescence response to multisine light intensity (amplitude:  $38\mu Em^{-2}s^{-1}$ , DC value:  $100\mu Em^{-2}s^{-1}$ ).

$$\theta = (\mathbf{K}_{\text{real}}^T \mathbf{W} \mathbf{K}_{\text{real}})^{-1} \mathbf{K}_{\text{real}}^T \mathbf{W} \mathbf{Y}_{\text{real}}. \quad (15)$$

Figure 4 shows the results of the Weighted Least Squares (WLS) method, where the parametric model achieves a good fit across both low and high frequencies.

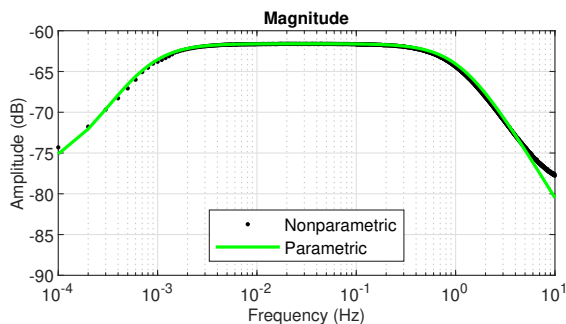


Fig. 4. Comparison of nonparametric and parametric (WLS) models for fluorescence response to multisine light intensity (amplitude:  $38\mu Em^{-2}s^{-1}$ , DC value:  $100\mu Em^{-2}s^{-1}$ ).

The next section explains how a set of linear models is used to represent nonlinear behavior through a Linear Parameter-Varying (LPV) modeling approach.

### Linear parameter-varying (LPV) model development

An LPV model representation for the in-silico data is developed based on a local approach. First, we present a set of local linear parametric models based on the FRF of the nonlinear system in Section 4.1. Section 4.3 formalizes the proposed scheduling variable for the LPV model. Section 4.4 outlines the state space representation of the proposed LPV model. Section 4.5 validates this LPV model via numerical simulations.

#### LPV model structure

By adopting a local modeling approach, the construction of an LPV model is based on a set of linear models that is interpolated based on a scheduling variable, as illustrated in Figure 5. In this framework, the parameters of the local linear models are parameterized as functions of the scheduling variable. Specifically in our case, the scheduling variable is the DC component of the light intensity

signal ( $u(t)$ ), which can either be determined offline or estimated in real-time using a low-pass filter.

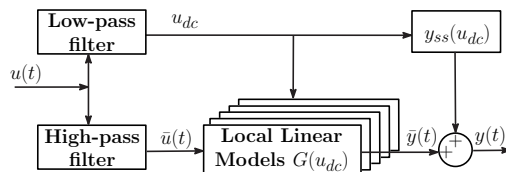


Fig. 5. LPV model structure.

Note that, for a linear model, its input and output are expressed in terms of perturbation coordinates. Hence, the perturbation input variable  $\bar{u}(t)$  can be calculated by subtracting the original input variable  $u(t)$  from its mean value (i.e., corresponding to the DC component of the light intensity  $u_{dc}$ ), or alternatively, it can be obtained in real time using a high-pass filter. For the output (chlorophyll fluorescence) of BDM (see in Section 2), the measured (original) output signal is given by

$$y(t) = \bar{y}(t) + y_{ss}(u_{dc}), \quad (16)$$

where the DC output  $y_{ss}(u_{dc})$  is parameterized in terms of a scheduling variable in the LPV model structure. In this work, the DC light intensity  $u_{dc}$  is set as the scheduling variable.

#### Local linear models

Following the non-parametric analysis outlined in the previous section, the Frequency Response Function (FRF) is calculated for various DC values ( $u_{dc}$ ). The DC values were varied from 100 to 1000 in increments of 50, generating 18 second-order linear and time-invariant models. Figure 6 presents the resulting magnitude bode plots for  $u_{dc} = 200, 400, 600$  and  $1000\mu Em^{-2}s^{-1}$ .

Figure 6 shows that the DC value substantially affects the FRF, as evident in the Bode magnitude plot, where the gain of the system varies with both frequency and changes in the DC value, affecting the parametric linear model.

#### Parametrization of the scheduling variable ( $u_{dc}$ )

The set of second-order transfer functions computed in previous sections can be written in continuous-time zero-pole-gain form as:

$$G(s) = \frac{\mathbf{K}(s - \mathbf{Z}_1)(s - \mathbf{Z}_2)}{(s - \mathbf{P}_1)(s - \mathbf{P}_2)}, \quad (17)$$

where  $\mathbf{K}$  is the gain of the system,  $\mathbf{Z}_1, \mathbf{Z}_2$  the zeros, and  $\mathbf{P}_1, \mathbf{P}_2$  the poles. The transfer function has equal order in both the numerator and the denominator, making it a proper transfer function. We guarantee also that the poles have negative real parts, which ensures stability.

The DC value will be used as the scheduling variable for the LPV model. To achieve this, a parameterization of the DC value is proposed where we derive functions that describe how the gain ( $K(u_{dc})$ ), poles ( $P_1(u_{dc}), P_2(u_{dc})$ ), and zeros ( $Z_1(u_{dc}), Z_2(u_{dc})$ ) change as a function of the DC value. The parameterization results for the gain are presented in Figure 7, where the coefficients of a fourth-degree interpolation polynomial were estimated, achieving an  $R^2 = 0.94$ .

Likewise, the parameterization results for the poles and zeros are presented in Figure 8, where the coefficients of a second-degree interpolation polynomial have been estimated. For all cases, the fitting exceeded  $R^2 = 0.97$ .

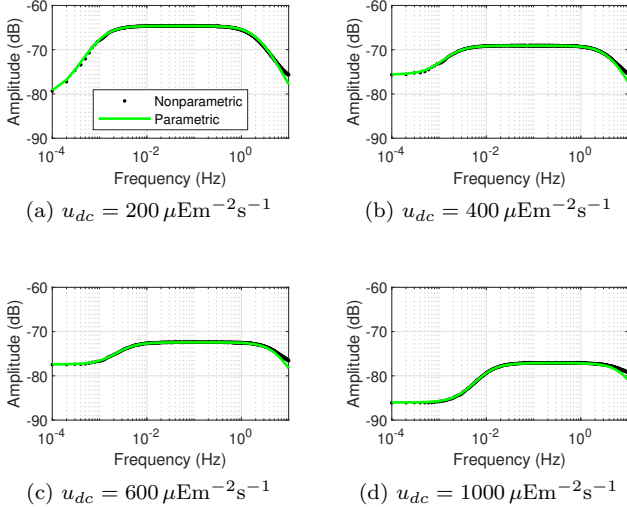


Fig. 6. Comparison of the FRF and the magnitude bode plots for parametric models for  $u_{dc} = 200, 400, 600$  and  $1000 \mu\text{Em}^{-2}\text{s}^{-1}$ .

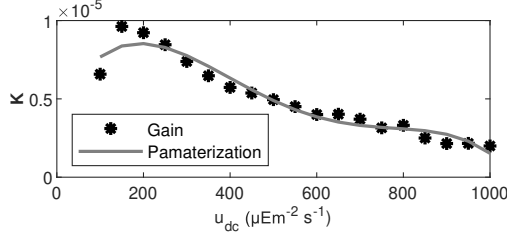


Fig. 7. Parametrization of the system gain with respect to the DC value.

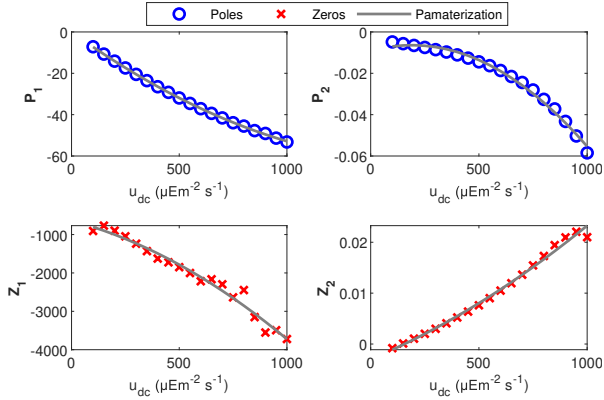


Fig. 8. Parametrization of the poles and zeros as a function of the DC value.

Additionally, it is necessary to parameterize the steady state value as a function of the scheduling variable  $u_{dc}$ . To achieve this, the steady-state response for constant light excitation was obtained across the same range of DC values. Consequently, the parameterization was performed using Fourier series up to the third harmonic. The result is shown in Figure 9, where the fundamental frequency is  $f_{0_{ss}} = 6.7 \times 10^{-5}$  Hz, indicating that  $y_{ss}(u_{dc})$  is being parameterized as a periodic signal.

Finally, the parameterization can be formulated by following non-linear static functions:

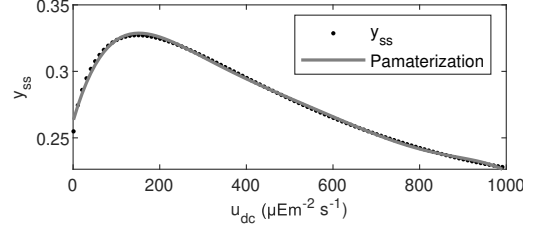


Fig. 9. Parametrization of the steady-state output as a function of the DC value.

$$\begin{aligned}
 K(u_{dc}) &= 3.97 \times 10^{-6} + \frac{u_{dc}}{5.62 \times 10^8} \dots \\
 &\dots - \frac{u_{dc}^2}{2.17 \times 10^{10}} + \frac{u_{dc}^3}{2.76 \times 10^{13}} - \frac{u_{dc}^4}{1.17 \times 10^{16}}, \\
 P_1(u_{dc}) &= -1.11 \times 10^{-2} - \frac{u_{dc}}{7.48 \times 10^2} + \frac{u_{dc}^2}{2.19 \times 10^5}, \\
 P_2(u_{dc}) &= -9.08 \times 10^{-3} + \frac{u_{dc}}{2.82 \times 10^5} - \frac{u_{dc}^2}{7.45 \times 10^8}, \\
 Z_1(u_{dc}) &= -637.87 - 1.49 u_{dc} - \frac{u_{dc}^2}{1.58 \times 10^3}, \\
 Z_2(u_{dc}) &= -2.98 \times 10^{-3} + \frac{u_{dc}}{1.78 \times 10^5} + \frac{u_{dc}^2}{8.46 \times 10^9}, \\
 y_{ss}(u_{dc}) &= a_0 + a_1 \sin(2\pi f_{0_{ss}} u_{dc}) \dots \\
 &\dots + b_1 \cos(2\pi f_{0_{ss}} u_{dc}) + a_2 \sin(4\pi f_{0_{ss}} u_{dc}) \dots \\
 &\dots + b_2 \cos(4\pi f_{0_{ss}} u_{dc}) + a_3 \sin(6\pi f_{0_{ss}} u_{dc}) \dots \quad (18) \\
 &\dots + b_3 \cos(6\pi f_{0_{ss}} u_{dc}), \quad (19)
 \end{aligned}$$

where  $a_0 = -20038$ ,  $a_1 = 7236.8$ ,  $b_1 = 29213$ ,  $a_2 = -5640.9$ ,  $b_2 = -10688$ ,  $a_3 = 1349.2$ ,  $b_3 = 1512.8$ .

### Space state representation of the LPV

The second-order transfer function with parameters varying depending on the DC value of the excitation signal can be formulated as follows:

$$G(s) = \frac{Y(s)}{U(s)} = \frac{b_0(u_{dc}) s^2 + b_1(u_{dc}) s + b_2(u_{dc})}{s^2 + a_1(u_{dc}) s + a_2(u_{dc})}, \quad (20)$$

where,

$$\begin{aligned}
 b_0(u_{dc}) &= K(u_{dc}), \\
 b_1(u_{dc}) &= (-Z_1(u_{dc}) - Z_2(u_{dc})) K(u_{dc}), \\
 b_2(u_{dc}) &= Z_1(u_{dc}) Z_2(u_{dc}) K(u_{dc}), \\
 a_1(u_{dc}) &= -P_1(u_{dc}) - P_2(u_{dc}), \\
 a_2(u_{dc}) &= P_1(u_{dc}) P_2(u_{dc}). \quad (21)
 \end{aligned}$$

Eq. (20) can be expressed in a block diagram as shown in Figure 10, where  $X(s)$  is called the states of the system.

Therefore, the transfer function can be rewritten as:

$$G(s) = \frac{Y(s)}{X(s)} \frac{X(s)}{U(s)}, \quad (22)$$

where  $\frac{X(s)}{U(s)}$  shows the dynamic relation between the input  $\bar{u}(t)$  and the state  $\bar{x}(t)$  through the differential equation in time domain:

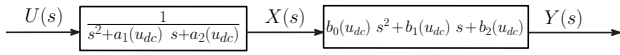


Fig. 10. Transfer function in a block diagram.

$$\ddot{\bar{x}}(t) + a_1(u_{dc})\dot{\bar{x}}(t) + a_2(u_{dc})\bar{x}(t) = \bar{u}(t). \quad (23)$$

Likewise,  $\frac{X(s)}{U(s)}$  in Eq. (22) shows relation between the state  $\bar{x}(t)$  and the output  $\bar{y}(t)$  by means of:

$$b_0(u_{dc})\ddot{\bar{x}}(t) + b_1(u_{dc})\dot{\bar{x}}(t) + b_2(u_{dc})\bar{x}(t) = \bar{y}(t). \quad (24)$$

Assume that  $\bar{x}_1(t) = \bar{x}(t)$  and  $\bar{x}_2(t) = \dot{\bar{x}}(t)$ . Then, Eqs. (23)–(24) can be written as a matrix system as:

$$\begin{aligned} \begin{bmatrix} \dot{\bar{x}}_1(t) \\ \dot{\bar{x}}_2(t) \end{bmatrix} &= \underbrace{\begin{bmatrix} 0 & 1 \\ -a_2(u_{dc}) & -a_1(u_{dc}) \end{bmatrix}}_{\mathbf{A}(u_{dc})} \underbrace{\begin{bmatrix} \bar{x}_1(t) \\ \bar{x}_2(t) \end{bmatrix}}_{\bar{\mathbf{x}}(t)} + \underbrace{\begin{bmatrix} 0 \\ 1 \end{bmatrix}}_{\mathbf{B}(u_{dc})} \bar{u}(t), \\ \bar{y}(t) &= \underbrace{\begin{bmatrix} b_2(u_{dc}) - (b_0(u_{dc})a_2(u_{dc})) \\ b_1(u_{dc}) - (b_0(u_{dc})a_1(u_{dc})) \end{bmatrix}}_{\mathbf{C}(u_{dc})} \underbrace{\begin{bmatrix} \bar{x}_1(t) \\ \bar{x}_2(t) \end{bmatrix}}_{\bar{\mathbf{x}}(t)} \dots \\ &\dots + \underbrace{\begin{bmatrix} b_0(u_{dc}) \end{bmatrix}}_{\mathbf{D}(u_{dc})} \bar{u}(t). \end{aligned} \quad (25)$$

Finally, the state space representation of the linear varying parameter model is given by:

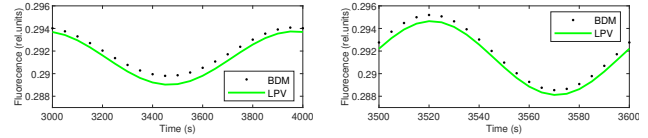
$$\begin{aligned} \dot{\bar{\mathbf{x}}}(t) &= \mathbf{A}(u_{dc}) \bar{\mathbf{x}}(t) + \mathbf{B}(u_{dc}) \bar{u}(t), \\ \bar{y}(t) &= \mathbf{C}(u_{dc}) \bar{\mathbf{x}}(t) + \mathbf{D}(u_{dc}) \bar{u}(t), \end{aligned} \quad (26)$$

where the state vector  $\bar{\mathbf{x}}(t)$  does not have a physical meaning and  $\bar{y}(t)$  is the perturbation variable of the output (chlorophyll fluorescence) of BDM corresponding to Eq. (16).

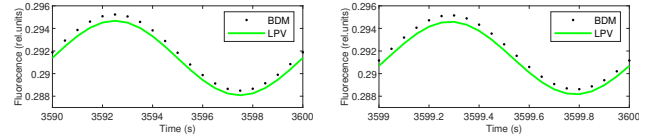
## Simulation results

In this section, we validate the LPV model through simulations and comparisons with the nonlinear BDM. Three distinct test cases are proposed to evaluate the performance of the LPV model under conditions different from those used during training. Since the LPV model was developed for steady-state conditions, the data from both the BDM and the LPV model were collected during the last period of 1 hour to ensure that transients had dissipated. The first set of results is presented in Figure 11, where the LPV model is tested at four different frequencies, using an oscillating light intensity with a DC value of  $u_{dc} = 420 \mu\text{Em}^{-2}\text{s}^{-1}$  and an amplitude of  $A = 10 \mu\text{Em}^{-2}\text{s}^{-1}$ .

Note that the DC value used in this case was not included in the training data. The results in Figure 11 show that the LPV model closely replicates the behavior of chlorophyll fluorescence generated by the BDM, with a  $R^2$  between 0.88 and 0.96. Furthermore, for the lower frequency,  $f = 1 \times 10^{-3}$ , a phase shift occurs, which is accurately captured by the LPV model. The LPV model was also validated at the same frequencies in a second case, using a higher DC value ( $u_{dc} = 860 \mu\text{Em}^{-2}\text{s}^{-1}$ ). Figure 12 compares the BDM and the LPV model, demonstrating that the LPV model closely fits the data for non-trained scenarios. Furthermore, note that the value ranges in Figures 11 and 12 differ, indicating that the LPV model effectively tracks changes in magnitude.

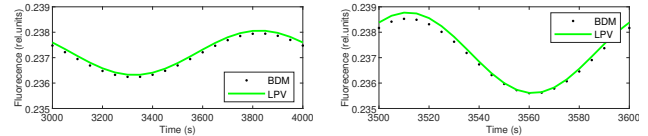


(a)  $f = 1 \times 10^{-3}$  Hz,  $R^2 = 0.88$ . (b)  $f = 1 \times 10^{-2}$  Hz,  $R^2 = 0.96$ .

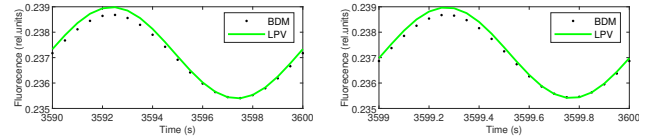


(c)  $f = 1 \times 10^{-1}$  Hz,  $R^2 = 0.96$ . (d)  $f = 1$  Hz,  $R^2 = 0.95$ .

Fig. 11. Comparison of fluorescence data at different frequencies, obtained using the BDM and LPV models, for a light oscillating excitation with a DC value of  $u_{dc} = 420 \mu\text{Em}^{-2}\text{s}^{-1}$  and an amplitude of  $A = 10 \mu\text{Em}^{-2}\text{s}^{-1}$ .



(a)  $f = 1 \times 10^{-3}$  Hz,  $R^2 = 0.88$ . (b)  $f = 1 \times 10^{-2}$  Hz,  $R^2 = 0.96$ .



(c)  $f = 1 \times 10^{-1}$  Hz,  $R^2 = 0.96$ . (d)  $f = 1$  Hz,  $R^2 = 0.95$ .

Fig. 12. Comparison of fluorescence data at different frequencies, obtained using the BDM and LPV models, for a light oscillating excitation with a DC value of  $u_{dc} = 860 \mu\text{Em}^{-2}\text{s}^{-1}$  and an amplitude of  $A = 10 \mu\text{Em}^{-2}\text{s}^{-1}$ .

Finally, in the last validation case, the LPV model is tested by applying a multi-frequency light intensity excitation by expanding (4) as follows:

$$u(t) = u_{dc} + u_1(t) + u_2(t) + u_3(t) + u_4(t), \quad (27)$$

where,

$$u_{dc} = 530 \mu\text{Em}^{-2}\text{s}^{-1}, \quad (28)$$

$$u_1(t) = 20 \sin(2\pi(1 \times 10^1)t),$$

$$u_2(t) = 20 \sin(2\pi(1 \times 10^{-1})t),$$

$$u_3(t) = 20 \sin(2\pi(1 \times 10^{-2})t),$$

$$u_4(t) = 20 \sin(2\pi(1 \times 10^{-3})t). \quad (29)$$

Note that the period of the signal  $u(t)$  corresponds to the lowest frequency  $1 \times 10^{-3}$  Hz in Eq. (28), resulting a period of 1000 seconds. The systems were simulated for a duration of 4000 seconds

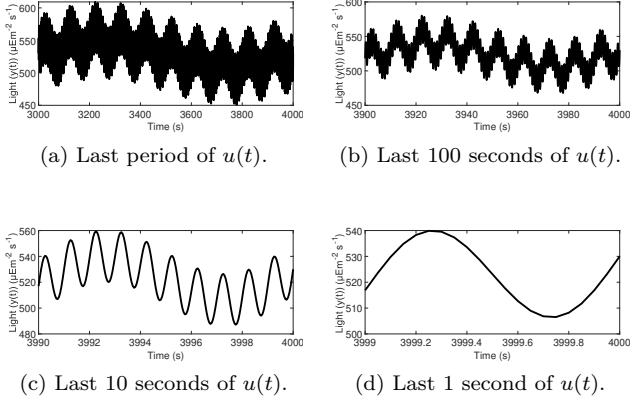


**Fig. 13.** Comparison of fluorescence data at different frequencies, obtained using the BDM and LPV models, for a light oscillating excitation with a DC value of  $u_{dc} = 860 \mu Em^{-2} s^{-1}$  and an amplitude of  $A = 10 \mu Em^{-2} s^{-1}$ .

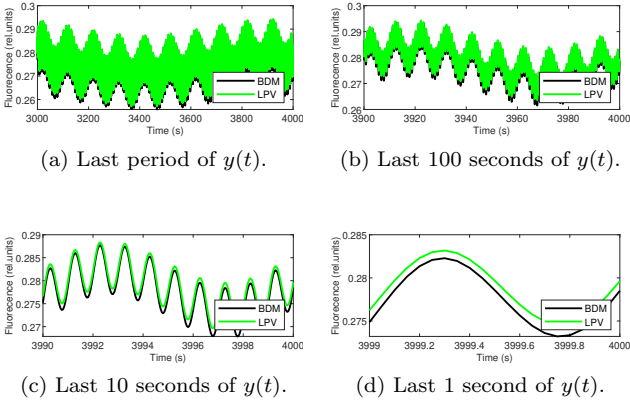


**Fig. 14.** Comparison of fluorescence data obtained using the BDM and the LPV model under multisine light intensity excitation.

to obtain the results, and we collected the chlorophyll fluorescence data from the last period for both the BDM and LPV models. The light intensity profile  $u(t)$  is shown in Figure 13, with its complete final period in Figure 13a. Figures 13b, 13c, and 13d present the last 100, 10, and 1 seconds of  $u(t)$ , respectively, highlighting its direct relationship with the frequencies in  $u_3$ ,  $u_2$ , and  $u_1$ .

The comparison between the fluorescence results for the BDM and LPV models is shown in Figure 14. The last period, with a fit of  $R^2 = 0.97$ , is presented in Figure 14a. To expose some frequency components, Figures 14b, 14c, and 14d illustrate the last 100, 10, and 1 seconds, respectively, to better relate the results to the light intensity excitation shown in Figure 13.

## Conclusion

This study has demonstrated the application of frequency-domain system identification techniques for modeling the dynamic regulation of photosynthesis under oscillating light, based on in-silico data generated from the Basic DREAM Model (BDM). The Best Linear Approximation (BLA) method successfully captured the local input-output dynamics, while the subsequent Linear Parameter-Varying (LPV) formulation provided a compact and scalable representation across a broad range of operating conditions (i.e., in terms of the DC component of light intensity). Furthermore, the use

of multisine excitation signals proved to be an efficient approach for characterizing the dynamical behavior of photosynthetic regulation within short experimental time frames.

These results provide a first step toward data-driven, control-oriented modeling of photosynthesis regulation. Future research will focus on validating the proposed framework using experimental plant data, thereby bridging the gap between in-silico modeling and practical applications in real-time phenotyping and optimized lighting strategies.

## Appendix A: Detailed description of BDM

This Appendix gives a more detailed representation of the the BDM framework presented in Section 2. The vector field  $f(\cdot)$  in Eq. (1a) describes the evolution of the state vector  $\mathbf{x}(t)$ , and is given by

$$f(\mathbf{x}(t), u(t), \Phi) = \begin{bmatrix} \frac{v_2(t) - v_1(t)}{2} + v_8(t) \\ b_H \left( \frac{v_{PSII}(t) + v_2(t)}{N_A V_L} - \frac{14}{3} \frac{V_S}{V_L} v_5(t) - v_7(t) \right) \\ v_3(t) - v_4(t) \\ v_5(t) - v_6(t) \\ v_{PSI}(t) - v_2(t) \end{bmatrix}, \quad (30)$$

where the associated rates for  $f(\cdot)$  in Eq. (30) are given by

$$\begin{aligned} v_1(t) &= k_1^+ \text{RCII}_{CL} x_1(t) \dots \\ &\dots - k_1^- (1 - \text{RCII}_{CL}) (\text{PQ}_{tot} - x_1(t)), \\ &= k_1^- (\text{RCII}_{CL} - 1) \text{PQ}_{tot} \dots, \\ &\dots + (k_1^+ \text{RCII}_{CL} + k_1^- (1 - \text{RCII}_{CL})) x_1(t) \end{aligned} \quad (31a)$$

$$\begin{aligned} v_2(t) &= k_2^+ (\text{PQ}_{tot} - x_1(t)) x_5(t) \dots \\ &\dots - k_2^- x_1(t) (1 - x_5(t)), \\ &= k_2^+ \text{PQ}_{tot} x_5(t) - k_2^- x_1(t) \dots \\ &\dots + (k_2^- - k_2^+) x_1(t) x_5(t), \end{aligned} \quad (31b)$$

$$v_3(t) = k_3 (1 - x_3(t)) \frac{1}{1 + \left( \frac{K_Q}{x_2(t)} \right)^n}, \quad (31c)$$

$$v_4(t) = k_4 x_3(t), \quad (31d)$$

$$v_5(t) = k_5 \left( A_{tot} - x_4(t) - \frac{x_4(t)}{c \text{EqP}} \left( \frac{H_{stroma}^+}{x_2(t)} \right)^{\frac{14}{3}} \right), \quad (31e)$$

$$v_6(t) = k_6 x_4(t), \quad (31f)$$

$$v_7(t) = k_7 (x_2(t) - H_{stroma}^+), \quad (31g)$$

$$v_8(t) = v_x(t) = k_8 (\text{PQ}_{tot} - x_1(t)), \quad (31h)$$

$$v_{PSII} = n_{PSII} \sigma_{II} (1 - \text{FQ}_{max} x_3(t)) \text{RCII}_{OP} L(t), \quad (31i)$$

$$v_{PSI} = n_{PSI} \sigma_I \frac{L_{1/2} L(t)}{(L_{1/2} + L(t))} (1 - x_5(t)). \quad (31j)$$

Note that based on Fuente et al. [2024], the following approximation holds:  $\text{RCII}_{OP} + \text{RCII}_{CL} = 1$ , where we have

$$\text{RCII}_{CL} = \frac{1}{1 + \frac{k_1^+ x_1(t)}{(1 - \text{FQ}_{max} x_3(t)) L(t) + k_1^- (\text{PQ}_{tot} - x_1(t))}}. \quad (32)$$

The vector field  $g(\cdot)$  in Eq. (1b) gives the trajectory of the output vector  $\mathbf{y}(t)$ , and is written as follows:

$$g(\mathbf{x}(t), u(t), \Phi) = \begin{bmatrix} g_1(\mathbf{x}(t), u(t), \Phi) \\ g_2(\mathbf{x}(t), u(t), \Phi) \\ g_3(\mathbf{x}(t), u(t), \Phi) \end{bmatrix}, \quad (33)$$

with

$$g_1(\mathbf{x}(t), u(t), \Phi) = (1 - \text{FQ}_{max} x_3(t)) \dots \dots \left( \frac{F_0}{F_V} + \text{RCII}_{CL} \right), \quad (34a)$$

$$g_2(\mathbf{x}(t), u(t), \Phi) = \frac{\text{FQ}_{max} x_3(t)}{(1 - \text{FQ}_{max} x_3(t))}, \quad (34b)$$

$$g_3(\mathbf{x}(t), u(t), \Phi) = \frac{v_{PSII}}{4} = \frac{(1 - \text{FQ}_{max} x_3(t)) \text{RCII}_{OPL}(t)}{4}. \quad (34c)$$

The following vector is constructed that consists of the BDM parameters used in Eqs. (30) – (34c) Portilla and Özkan [2024]:

$$\Phi = \begin{bmatrix} kI & k_1^+ & k_1^- & k_2^+ & k_2^- & k_3 & k_4 & \dots \\ \dots & k_5 & k_6 & k_7 & k_8 & \dots \\ \dots & A_{tot} & b_H & \text{FQ}_{max} & n & \dots \\ \dots & \text{cEqP} & K_Q & \text{PQ}_{tot} \end{bmatrix}. \quad (35)$$

The BDM parameters for the vector fields are listed in Fuente et al. [2024].

## Competing interests

No competing interest is declared.

## Author contributions statement

C.P. is for writing – original draft, visualization, validation, software, methodology, and conceptualization. A.G.A, R.A., and C.A.G.-P. are for writing – review and editing. L.Ö. is for writing – review and editing, supervision, methodology, and conceptualization.

## Acknowledgments

The work was funded by HORIZON-EIC-2021-PATHFINDER OPEN project DREAM with the grant agreement no. 101046451. The authors would like to acknowledge David Fuente, Dusan Lazar and Ladislav Nedbal for their technical support in relation to the Basic Dream Model.

## References

A. A. Bachnas, R. Tóth, J. H. A. Ludlage, and A. Mesbah. A review on data-driven linear parameter-varying modeling approaches: A high-purity distillation column case study. *Journal of Process Control*, 24(4):272–285, Apr. 2014. ISSN 0959-1524. doi: <https://doi.org/10.1016/j.jprocont.2014.01.015>. URL <https://www.sciencedirect.com/science/article/pii/S0959152414000390>.

N. R. Baker. Chlorophyll fluorescence: a probe of photosynthesis in vivo. *Annual review of plant biology*, 59:89–113, 2008. ISSN 1543-5008. doi: 10.1146/annurev.arplant.59.032607.

092759. URL <http://arjournals.annualreviews.org/doi/full/10.1146/annurev.arplant.59.032607.092759>.

F. S. Bala, M. D. O’Toole, and B. D. Grieve. A system identification approach to modelling chlorophyll fluorescence response to dynamic light conditions. In *2025 IEEE Sensors Applications Symposium (SAS)*, pages 1–6, 2025. doi: 10.1109/SAS65169.2025.11105194.

D. I. C. Pahl-Wostl. *Dyphora*-a dynamic model for the rate of photosynthesis of algae. *Journal of Plankton Research*, 12(6):1207–1221, Nov. 1990. doi: <https://doi.org/10.1093/plankt/12.6.1207>.

T. P. Dobrowiecki and J. Schoukens. Linear approximation of weakly nonlinear MIMO systems. *IEEE Transactions on Instrumentation and Measurement*, 56(3):887–894, 2007. doi: 10.1109/TIM.2007.894898.

P. H. C. Eilers and J. C. H. Peeters. A model for the relationship between light intensity and the rate of photosynthesis in phytoplankton. *Ecological Modelling*, 42(3-4):199–215, Sept. 1988. doi: [https://doi.org/10.1016/0304-3800\(88\)90057-9](https://doi.org/10.1016/0304-3800(88)90057-9).

D. Fuente, M. Orlando, B. Bailleul, L. Jullien, D. Lazar, and L. Nedbal. A mathematical model to simulate the dynamics of photosynthetic light reactions under harmonically oscillating light. *Plant Physiology and Biochemistry*, 217:109138, 2024. ISSN 0981-9428. doi: <https://doi.org/10.1016/j.plaphy.2024.109138>. URL <https://www.sciencedirect.com/science/article/pii/S0981942824008064>.

J. M. Kenneth L. Denman. Modelling the time dependent photoadaptation of phytoplankton to fluctuating light. *Elsevier Oceanography Series*, 42:341–359, 1986. doi: [https://doi.org/10.1016/S0422-9894\(08\)71054-7](https://doi.org/10.1016/S0422-9894(08)71054-7).

V. Laurain, M. Gilson, R. Tóth, and H. Garnier. Refined instrumental variable methods for identification of LPV Box-Jenkins models. *Automatica*, 46(6):959–967, 2010. ISSN 0005-1098. doi: <https://doi.org/10.1016/j.automatica.2010.02.026>. URL <https://www.sciencedirect.com/science/article/pii/S0005109810000981>.

D. Lazar, Y. Niu, and L. Nedbal. Insights on the regulation of photosynthesis in pea leaves exposed to oscillating light. *Journal of Experimental Botany*, 73(18):6380–6393, 08 2022. ISSN 0022-0957. doi: 10.1093/jxb/erac283. URL <https://doi.org/10.1093/jxb/erac283>.

M. Lovera, M. Bergamasco, and F. Casella. *LPV modelling and identification: an overview*, chapter 1, pages 3–24. Springer Berlin Heidelberg, Berlin, Heidelberg, 2013. ISBN 978-3-642-36110-4. doi: 10.1007/978-3-642-36110-4\_1. URL [https://doi.org/10.1007/978-3-642-36110-4\\_1](https://doi.org/10.1007/978-3-642-36110-4_1).

L. Nedbal and D. Lazar. Photosynthesis dynamics and regulation sensed in the frequency domain. *Plant Physiology*, 187(2):646–661, 07 2021. ISSN 0032-0889. doi: 10.1093/plphys/kiab317. URL <https://doi.org/10.1093/plphys/kiab317>.

Y. Niu, D. Lazar, A. R. Holzwarth, D. M. Kramer, S. Matsubara, F. Fiorani, H. Poorter, S. D. Schrey, and L. Nedbal. Plants cope with fluctuating light by frequency-dependent nonphotochemical quenching and cyclic electron transport. *New Phytologist*, 239(5):1869–1886, 2023. doi: <https://doi.org/10.1111/nph.19083>. URL <https://nph.onlinelibrary.wiley.com/doi/abs/10.1111/nph.19083>.

T. Ogawa. Simple oscillations in photosynthesis of higher plants. *Biochimica et Biophysica Acta (BBA) - Bioenergetics*, 681(1):103–109, 1982. ISSN 0005-2728. doi: [https://doi.org/10.1016/0005-2728\(82\)90283-3](https://doi.org/10.1016/0005-2728(82)90283-3). URL <https://www.sciencedirect.com/science/article/pii/0005272882902833>.

R. W. Pearcy, L. J. Gross, and D. He. An improved dynamic model of photosynthesis for estimation of carbon gain in sunfleck light

- regimes. *Plant, Cell & Environment*, 20:411–424, 1997. doi: <https://doi.org/10.1046/j.1365-3040.1997.d01-88.x>.
- R. Pintelon and J. Schoukens. *System identification: a frequency domain approach*. Wiley-IEEE Press, Piscataway, NJ, 2012. ISBN 9781118287422. URL <https://ieeexplore.ieee.org/servlet/opac?bknumber=6198969>.
- R. Pintelon and J. Schoukens. FRF measurement of nonlinear systems operating in closed loop. *IEEE Transactions on Instrumentation and Measurement*, 62(5):1334–1345, 2013. doi: 10.1109/TIM.2012.2220033.
- C. Portilla and L. Özkan. A first- and second-generation DREAM dynamical model of photosynthesis regulation in light-acclimated algae and plants. Technical report, 2024.
- M. R. Roussel and A. U. Igamberdiev. Dynamics and mechanisms of oscillatory photosynthesis. *Biosystems*, 103(2):230–238, 2011. ISSN 0303-2647. doi: <https://doi.org/10.1016/j.biosystems.2010.07.020>. URL <https://www.sciencedirect.com/science/article/pii/S0303264710001292>. Computational Models of Photosynthesis.
- N. Salvatori, F. Carteni, F. Giannino, G. Alberti, S. Mazzoleni, and A. Peressotti. A system dynamics approach to model photosynthesis at leaf level under fluctuating light. *Frontiers in Plant Science*, Volume 12 - 2021, 2022. ISSN 1664-462X. doi: 10.3389/fpls.2021.787877. URL <https://www.frontiersin.org/journals/plant-science/articles/10.3389/fpls.2021.787877>.
- J. Schoukens and L. Ljung. Nonlinear system identification: a user-oriented road map. *IEEE Control Systems Magazine*, 39(6):28–99, 2019. doi: 10.1109/MCS.2019.2938121.
- J. Schoukens, R. Pintelon, and Y. Rolain. *Mastering system identification in 100 exercises*. Wiley-IEEE Press, Piscataway, NJ, 2012. ISBN 9780470936986. URL <https://ieeexplore.ieee.org/servlet/opac?bknumber=6183553>.
- M. Schoukens and P. M. J. van den Hof. Detecting nonlinear modules in a dynamic network: a step-by-step procedure. *IFAC-PapersOnLine*, 51(15):593–597, 2018. ISSN 2405-8963. doi: <https://doi.org/10.1016/j.ifacol.2018.09.224>. URL <https://www.sciencedirect.com/science/article/pii/S2405896318318962>. 18th IFAC Symposium on System Identification SYSID 2018.
- M. Schoukens, R. Pintelon, T. P. Dobrowiecki, and J. Schoukens. Extending the best linear approximation framework to the process noise case. *IEEE Transactions on Automatic Control*, 65(4):1514–1524, 2020. doi: 10.1109/TAC.2019.2923038.
- X. Wu and J. C. Merchuk. A model integrating fluid dynamics in photosynthesis and photoinhibition processes. *Chemical Engineering Science*, 56(11):3527–3538, June 2001. doi: [https://doi.org/10.1016/S0009-2509\(01\)00048-3](https://doi.org/10.1016/S0009-2509(01)00048-3).